Phonon-mediated superconductivity near the lattice instability in hole-doped hydrogenated monolayer hexagonal boron nitride

Takat B. Rawal,[1,*] Ling-Hua Chang,[1] Hao-Dong Liu,[2] Hong-Yan Lu,[2,†] and C. S. Ting[1]
[1]*Texas Center for Superconductivity and Department of Physics, University of Houston, Houston, Texas 77204, USA*
[2]*School of Physics and Physical Engineering, Qufu Normal University, Qufu 273165, China*

(Received 28 September 2021; accepted 2 May 2022; published 19 May 2022)

Employing the density functional theory with local density approximation, we show that the fully hydrogenated monolayer-hexagonal boron nitride (H_2BN) has a direct band gap of 2.96 eV in the blue-light region, while the pristine *h*-BN has a wider indirect band gap of 4.78 eV. The hole-doped H_2BN is stable at low carrier density (n) but becomes dynamically unstable at higher n. We predict that it is a phonon-mediated superconductor with a transition temperature (T_c) which can reach ∼31 K at n of 1.5×10^{14} holes cm^{-2} near the lattice instability. The T_c could be enhanced up to ∼82 K by applying a biaxial tensile strain at 6% along with doping at n of 3.4×10^{14} holes cm^{-2} close to a new lattice instability.

DOI: 10.1103/PhysRevMaterials.6.054003

I. INTRODUCTION

Two-dimensional (2D) electron system such as graphene has attracted a lot of attention since its atomic structure in the form of a single layer was realized experimentally [1]. Owing to the exceptional electronic and other properties, it may be used for a wide range of applications [2–8], including superconducting quantum circuits for quantum computing [8]. By tuning its electronic properties, one may remarkably achieve and adjust the superconductivity (SC). Very recently, robust SC has been observed for the magic angle twisted trilayer graphene [9] with T_c up to 2.1 K [10]. For twisted bilayer graphene, the T_c up to 1.7 K has been reported [11,12]. The SC may arise in twisted trilayer or bilayer graphene from interlayer interactions which are missing in its monolayer limit, albeit the full understanding of the mechanism behind SC in a graphenelike, 2D system is not well developed.

The study of another 2D system like monolayer-hexagonal boron nitride (*h*-BN) becomes popular. The pristine compound has a honeycomb lattice structure similar to that of graphene. It has been predicted [13] that the monolayer *h*-BN is an insulator with an indirect band gap of 4.47 eV, but recent experiments [14] demonstrate that it has a gap of ∼5 eV. By employing the first-principles methods as in prior studies on 2D materials [15–19], the doped *h*-BN has been predicted to be a phonon-mediated superconductor with $T_c \sim 41$ K under an applied biaxial tensile strain (BTS) together with doped holes (5.3×10^{14} holes cm^{-2}) [20]. The doped holes may come from either gating or chemical doping. The gating approach is similar to the case for biaxial-tensile-strained and doped graphene (4.0×10^{14} holes cm^{-2}) which shows the SC with $T_c \sim 30$ K [21]. By means of chemical doping of Ca, Ba, and Sr atoms, one may theoretically obtain SC in monolayer *h*-BN with T_c ranging from ∼1 to 10 K [22]. The bilayer *h*-BN with an intercalated Li atom has also been predicted to show SC with different T_c (<25 K) [23,24]. Despite some efforts being devoted to developing the fundamental understanding of phonon-mediated SC in doped *h*-BN, the electronic structure, lattice stability, and SC in H_2BN (fully hydrogenated monolayer *h*-BN) have not been studied. The focus of this paper is to investigate these properties in pristine and hole-doped H_2BN by adopting an approach similar to the one implemented in previous studies on graphane [16] and graphene [21].

In this paper, we apply methods based on the first-principles density functional theory (DFT) with local density approximation (LDA) [25] plus plane waves and pseudopotential approaches [26–28] and the density functional perturbation theory (DFPT) [29]. Firstly, we study the structural and electronic properties of pristine *h*-BN and H_2BN. We found that the undoped H_2BN has a direct band gap of 2.96 eV in the blue-light region. The full hydrogenation of *h*-BN gives rise to a transition from indirect [13] to direct band gap. The subsequent modification in electronic properties by hole doping gives the metallicity with the finite density of states at Fermi level. We show that there exist no negative phonon frequencies in k space for doped H_2BN with n varying from 0 up to 1.5×10^{14} holes cm^{-2}, indicating the stability of the lattice in this doping range. But as $n > \sim 1.55 \times 10^{14}$ holes cm^{-2}, negative frequencies begin to appear near Γ point suggesting the lattice instability. For stable lattice structures, we evaluate the electron-phonon (e-ph) interaction strength λ in hole-doped H_2BN using DFPT [29].

Taking advantage of the high-phonon frequencies and the soft phonon modes near the lattice instability (LI), we examine the existence of SC in hole-doped H_2BN and estimate its T_c. Our methods are based upon the Bardeen-Cooper-Schrieffer (BCS) theory [30] and the Eliashberg approach plus its extended versions [31–35]. The modified Eliashberg theory [32,34] has been widely employed to understanding the BCS

*tbrawal@gmail.com
†hylu@qfnu.edu.cn

superconductivity in metallic materials. We show that with hole doping at n of 1.5×10^{14} holes cm^{-2}, the doped H_2BN exhibits phonon-mediated SC with T_c above the boiling point of liquid hydrogen. The T_c can be enhanced further above liquid nitrogen temperature when we apply BTS at 6% and increase n up to 3.4×10^{14} holes cm^{-2}.

II. COMPUTATIONAL DETAILS

A. Density functional theory

We perform first-principles DFT calculations using LDA functional [25] plus plane waves and pseudopotentials approaches [28] implemented in Quantum Espresso (QE) code [36]. The interaction between ions and electrons are treated using norm-conserving pseudopotentials [26,27], which take into account B $2s^2, 2p^1$, N $2s^2, 2p^3$, and H $1s^1$ as valence electrons. We use the LDA for describing the exchange-correlation of electrons since it reproduces very well the geometrical structure of h-BN [37,38]. To achieve the convergence of total energy below 0.07 mRy per atom, we use an energy cutoff of 80 Ry for the plane waves expansion. For the electronic integration during self-consistent cycles, we describe the fractional occupations using the first-order Methfessel-Paxton method [39]. To simulate the monolayer h-BN, we use (1×1) unit cell containing 16 Å of vacuum which is found sufficient to prevent the artificial electrostatic interaction between layers along z direction. We initially place hydrogen atoms alternatively on both sides of the h-BN plane. We denote the corresponding geometry of the fully hydrogenated monolayer h-BN as H_2BN. For structural relaxations, we use the $24 \times 24 \times 1$ k-mesh with automatic generation of k points according to the Monkhorst-Pack scheme [40]. The positions of atoms are optimized using the Broyden Fletcher Goldfarb Shanno (BFGS) quasi-newton algorithm so that forces on each atom reach below 10^{-7} Ry/a.u.

In the rigid-band approximation [41], we simulate the hole doping into H_2BN through replacing the total valence electrons per N atom per unit cell ($Z_B + Z_N + 2Z_H = 3 + 5 + 2 = 10$e) by $(10 - y)$e, where y represents the number of holes per unit cell. The similar method has been adopted in prior studies on p-doped graphane [16].

B. Lattice-dynamical and superconducting properties

To compute phonon modes and dispersions as well as e-ph interaction, we use DFPT [29] implemented in QE [36]. The total number of perturbations due to atomic displacements to be treated amounts to 3N, where N=Number of atoms, i.e., 12 for the (1×1) H_2BN monolayer. We calculate the phonon frequencies using the linear-response technique within DFPT. For calculations of e-ph interaction, we adopt a scheme of interpolation over the Brillouin zone (BZ). We compute the e-ph coupling using the momentum k mesh of $192 \times 192 \times 1$. Such dense k-point mesh is found to sufficient for calculating the electronic density of states (DOS). For calculation of phonon DOS, we use a dense $110 \times 110 \times 1$ mesh of q points with ndos value of 2500. We checked in detail the convergence of λ for several values of smearing for both electrons and phonons.

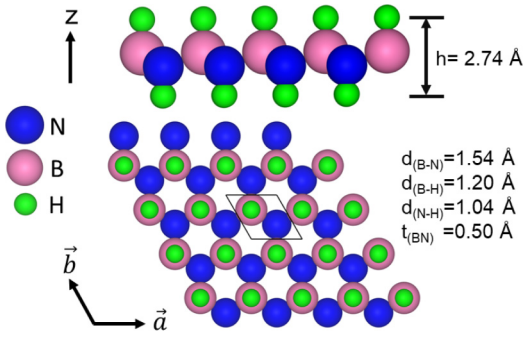

FIG. 1. DFT-optimized structure of an undoped H_2BN monolayer: side (top panel) and top (bottom panel) views. The height (h) of the H_2BN monolayer is 2.74 Å. Here, the height is defined as $h = d_{(B-H)} + d_{(N-H)} + t_{(BN)}$, where $d_{(B-H)}$ is the bond length between B and H atoms, and $d_{(N-H)}$ is the bond length between N and H atoms, and $t_{(BN)}$ is the thickness of a reconstructed BN layer. Alternatively, the height of the monolayer can be defined as the difference in z-position of the two hydrogen atoms, H_B and H_N, i.e., $Z(H_B)$ $Z(H_N)$, where $Z(H_B)$ and $Z(H_N)$ represent the z positions of hydrogen atoms bonded to boron and nitrogen atom, respectively. The (1×1) unit cell of the H_2BN is shown by black lines (bottom).

We calculate the T_c using the modified McMillan equation [33–35] and Coulomb parameter μ^*=0.13 [34,42]. The choice of other values of μ^* do not affect qualitatively our conclusions.

III. RESULTS AND DISCUSSION

A. Structural properties

Upon relaxation of monolayer h-BN with hydrogen atom attached to each B and N atom on both sides of the monolayer plane, the planar h-BN layer is reconstructed and the geometrical structure of fully hydrogenated monolayer h-BN, which we call H_2BN, becomes similar to that of graphane [43]. We show the DFT-optimized structure of H_2BN in Fig. 1. The optimized lattice parameter of the fully hydrogenated (1×1) h-BN is 2.56 Å, which is deviated by ∼2% from that of crystalline h-BN (2.51 Å) [44]. The thickness of H_2BN monolayer is estimated to be 2.74 Å.

B. Electronic properties

Figure 2 shows the calculated electronic band structures of monolayer h-BN (pristine) and undoped H_2BN along the high-symmetry directions in the first BZ. The hydrogenation of h-BN modifies its electronic structure along with a band gap [Fig. 2(b)] owing to the charge redistributions that trigger electrons to be piled up at different potential regions from those of monolayer pristine h-BN. The valence band (VB) dispersion of H_2BN is found different from that of monolayer h-BN. The periodicity length of the Brillouin zone of this system differs from that of h-BN, and it is due to the different periodic potential of H_2BN with only six symmetry operations (i.e., 1/2 of 12 symmetry operations in the pristine monolayer h-BN. The details of the symmetry operations for both model systems are provided in Table III in the Appendix). The valence band (VB) maximum occurs at K point for h-BN whereas it occurs at Γ point for H_2BN. The calculated

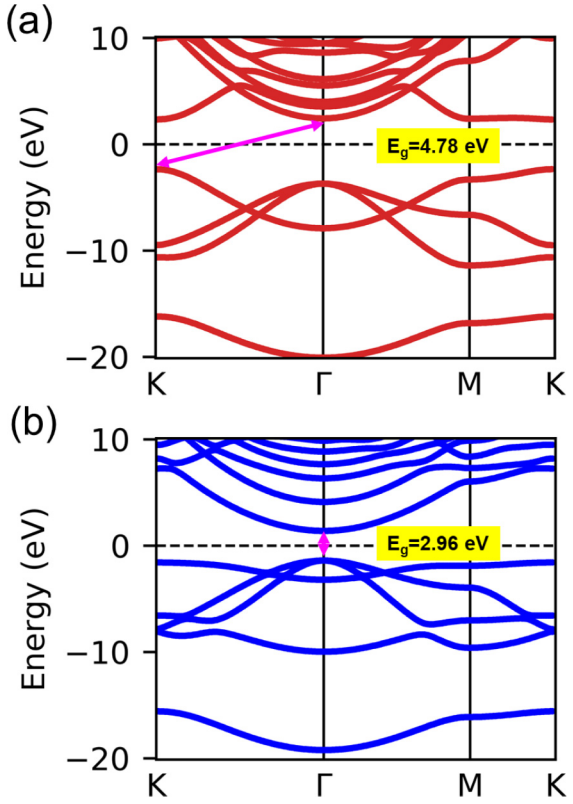

FIG. 2. Electronic band structures of monolayer (a) *h*-BN and (b) H_2BN (undoped) along the high-symmetry directions in the first Brillouin zone. The chemical potential is set to zero. In inset, the E_g represents the energy gap between the valence band maximum and the conduction band minimum.

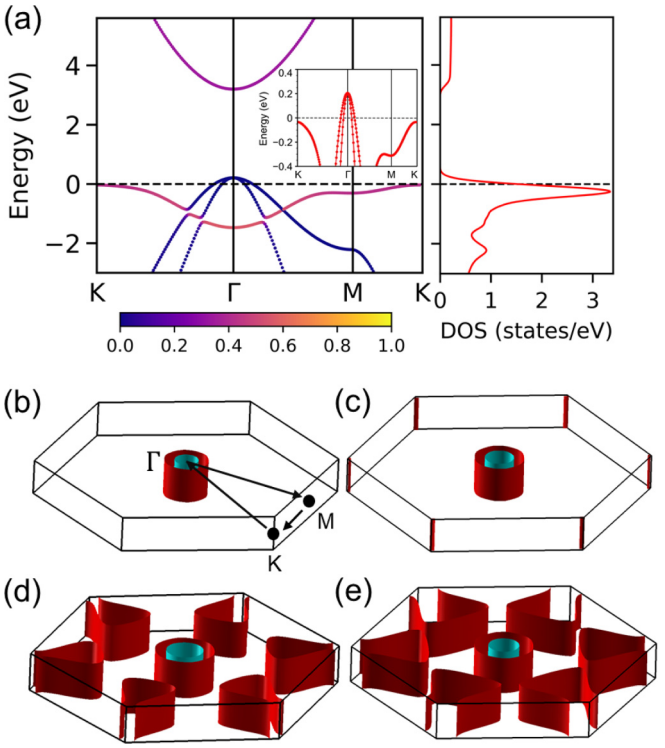

FIG. 3. (a) Electronic band structure along high-symmetry directions in the first Brillouin zone (left) and the electronic density of states (right) of the hole-doped H_2BN with the carrier density of 1.0×10^{14} holes cm^{-2}. The Fermi level is set to zero. The color bar represents the projections of H s states to bands. For clarity of the effect of hole doping, the band structure for the small energy window around the Fermi level is also shown in inset. [(b) and (c)] Fermi surfaces in the first Brillouin zone of the doped H_2BN with the carrier density (n) of (b) 1.0×10^{14} and (c) 1.5×10^{14} holes cm^{-2}. In (b), the high-symmetry k-point directions (K-Γ-M-K) are also depicted by arrow. The Fermi surfaces of strained H_2BN with BTS of 6% are shown for n of: (d) 2.0×10^{14} and (e) 3.4×10^{14} holes cm^{-2}.

indirect band gap of *h*-BN monolayer at the level of DFT generalized-gradient approximation is 4.47 eV [13], whereas the most recent experiment reveals the gap of ∼5 eV [14]. Our calculated indirect band gap of *h*-BN without hydrogenation at the LDA level is, however, 4.78 eV [Fig. 2(a)]. Our result is thus in better accord with the experiment. When monolayer *h*-BN is fully hydrogenated, the LDA band gap reduces to 2.96 eV [Fig. 2(b)]. Both VB maximum and conduction band minimum occur at the BZ center, and therefore there is a crossover from indirect to direct band gap. Thus, we can tune the gap of the *h*-BN from indirect to direct with a value changed by 1.82 eV. Such electronic modification may be useful for exploiting H_2BN in optical quantum devices. The projected electronic DOS for undoped *h*-BN and H_2BN are respectively shown in Figs. 8(a) and 8(b) in the Appendix.

Figure 3(a) shows the electronic band structure of hole-doped H_2BN with n of 1.0×10^{14} holes cm^{-2} and also its total DOS (This hole concentration can be obtained by replacing 0.06% of N atoms with the same amount of B atoms, and such hole-doped compound can be represented by $H_2B_{(1+x)}N_{(1-x)}$ with $x = 0.006$). The chemical potential labeled by 0 eV crosses the VB maximum near the BZ center. Thus, it creates two hole pockets: one with a lighter mass and the other with a heavier mass. With the doping increased to 1.5×10^{14} holes cm^{-2}, the chemical potential moves downward toward the lower energy and crosses the VB maximum near the high-symmetry K point. The Fermi surfaces at these doping levels are respectively shown in Figs. 3(b) and 3(c). For these doping levels, Fermi surfaces are found to appear near the Γ point. From the calculated projected density of states of hole-doped H_2BN (see Fig. 9 in the Appendix), it is seen that the bands contribute strongly to the DOS at the Fermi level. The occupied σ-bonding bands should promote remarkably the e-ph coupling (EPC) in H_2BN, as is the case for hydrogenated MgB_2 [45] and graphane (fully hydrogenated graphene) [16].

C. Lattice dynamical properties

We examine the dynamical stability of the undoped and hole-doped H_2BN systems without strain. In Fig. 4, we show the phonon frequency dispersion of the doped H_2BN with n of 1.0×10^{14} holes cm^{-2}, and compare it with that of undoped H_2BN for the selected energy range. Several optical phonon modes at the Γ point are shown in Fig. 10 in the Appendix. The hole doped H_2BN exhibits a smooth softening of optical and acoustic branches around the zone center when compared with those of undoped H_2BN. The optical B-N stretching mode is softened the most when H_2BN is doped (indicated by

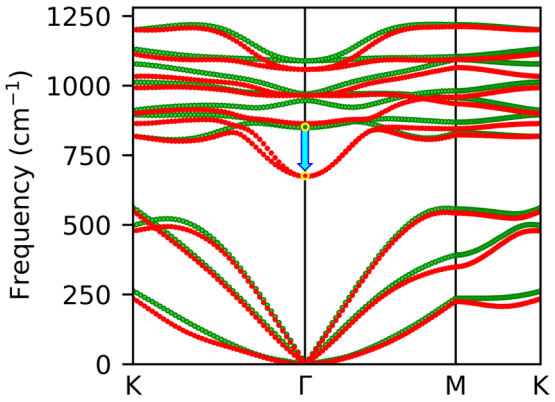

FIG. 4. Comparison of phonon dispersion of the undoped H_2BN (green trace) and hole-doped H_2BN with carrier density of 1.0×10^{14} holes cm^{-2} (red) for the selected frequency range up to 1280 cm^{-1}, showing the Kohn anomaly [46].

arrow in Fig. 4). The hole doped H_2BN system with a suitable density of hole carriers thus exhibits the Kohn anomaly [46] in phonon dispersion. These results suggest that upon further doping, these optical and acoustic modes may be further softened until the lattice becomes dynamically unstable. Several doping dependent optical modes at the Γ point are shown in Table IV in the Appendix.

Figure 5 shows the resulting phonon band structure and phonon DOS of hole-doped H_2BN with n of 1.0×10^{14} holes cm^{-2}. The calculated phonon spectra without imaginary frequencies substantiate the dynamical stability of the doped H_2BN. The phonon dispersion of the hole-doped H_2BN exhibits kinks at $q = 2k_F$ (Figs. 4 and 5) because of the Kohn anomaly [46] and this anomaly has an effect on the e-p interaction. As shown in Fig. 4, the phonon modes softening occurs at and around Γ point, similar to the doped graphane [16]. By increasing the hole density, the optical B-N stretching mode softening can be increased. In the case of doped H_2BN with different hole carrier density, the optical B-N stretching mode softening takes place with the frequency changing from 850 to 675 cm^{-1} for a carrier density 1.0×10^{14} holes cm^{-2}, and from 850 to 647 cm^{-1} for 1.5×10^{14} holes cm^{-2} (see Table IV in the Appendix).

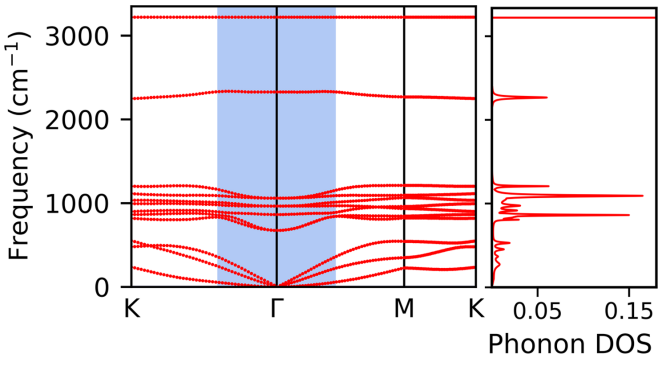

FIG. 5. Phonon frequency dispersion along high-symmetry directions of the first Brillouin zone (left) and phonon density of states (right) of the hole-doped H_2BN with n of 1.0×10^{14} holes cm^{-2}. The modes with $q < 2k_F$ are shaded.

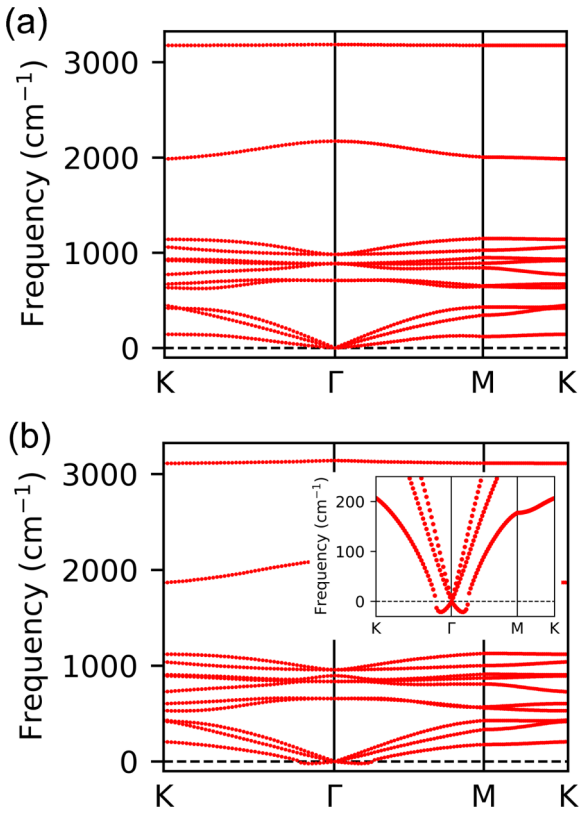

FIG. 6. Phonon frequency dispersion of the strained and doped H_2BN models under 6% BTS with the carrier densities of (a) 3.4×10^{14} and (b) 3.5×10^{14} holes cm^{-2}. For the latter carrier density, the doped H_2BN has negative frequencies around the Γ point, as shown in inset.

The H-related in-plane motion gives rise to three different frequencies with higher phonon DOS around 1000 cm^{-1} in Fig. 5. The softer modes with frequencies near 1059 cm^{-1} give rise to the highest phonon DOS. In addition, there are two other DOS peaks, one at ∼1205 cm^{-1} and the other at ∼864 cm^{-1}. Although the phonon DOS is relatively small near 965 cm^{-1}, the optical frequencies are related to the in-plane motion of H atoms (see Fig. 10 in the Appendix) and thus should effectively contribute to the e-ph interaction. The contribution of these modes to the e-ph interaction has been theoretically studied previously [47]. With no strain, the lattice is found to dynamically stable for the carrier density up to 1.5×10^{14} holes cm^{-2} [see Fig. 11(a) in the Appendix]. At $n = 1.6 \times 10^{14}$ holes cm^{-2}, the lattice becomes unstable with negative frequencies appearing in one of the acoustic branches near the zone center [see Fig. 11(b) in the Appendix]. Here, we study the phonon-mediated SC up to the hole density near the LI.

The onset of the LI appears to occur at $\sim 1.55 \times 10^{14}$ holes cm^{-2} under no BTS. It may arise from the fact that the Fermi level is trying to cross the top of the VBs at K points and to create the hole pockets. Near K points the hole bands are dominantly originated from B-2p_z and H-1s orbitals which contribute a high electronic DOS peak (see Fig. 9 in Appendix).

TABLE I. Comparison of selected optical phonon frequencies (given in unit of cm^{-1}) at the BZ center of undoped and doped H_2BN systems under BTS of 6%. The hole carrier densities (in unit of 10^{14} holes cm^{-2}) are given in parenthesis. The normal modes are provided, and numbers in parenthesis represent degree rotation. The in-plane H, out-of-plane B-N, and B-N stretching modes have E, A_1, and E' symmetry, respectively.

Normal modes	H_2BN (0.0)	H_2BN (2.0)	H_2BN (3.4)
In-plane H (0)	1052	997	985
In-plane H (90)	1052	997	985
In-plane H (30)	953	912	886
In-plane H (120)	953	912	886
Out-of-plane B-N	925	886	885
B-N stretching (0)	734	709	707
B-N stretching (90)	734	709	707

D. Effect of biaxial tensile strain

By applying BTS [20,21], defined by $\epsilon=(a-a_0)/a_0 \times 100\%$ where a and a_0 are the in-plane lattice constants for strained and unstrained (a_0=2.56 Å) cases respectively, we can push the LI to the higher n. In Fig. 6, we compare the phonon frequency dispersion of strained and doped H_2BN with n of 3.4×10^{14} and 3.5×10^{14} holes cm^{-2}. If $\epsilon = 6\%$ is applied, the doped system with n of 3.4×10^{14} holes cm^{-2} that is unstable at $\epsilon = 0$, now becomes stable [Fig. 6(a)]. As shown, the H_2BN lattice with a BTS up to 6% is found to be dynamically stable up to this n. With further increasing of the n up to 3.5×10^{14} holes cm^{-2}, however, the doped H_2BN exhibits the negative frequencies near Γ [Fig. 6(b) and inset], thus indicating the system to be dynamically unstable.

For the doping of 3.4×10^{14} holes cm^{-2}, both the optical phonon and acoustic branches related to the in-plane displacements of B and N atoms and the in-plane motion of H atoms may give rise to the strong e-ph coupling.

In Table I, we present the selected phonon modes calculated at the center of BZ of the hole-doped H_2BN under BTS of 6% up to n of 3.4×10^{14} holes cm^{-2}. The optical modes associated with H in-plane motion, are found to be softer with frequencies of 985 cm^{-1} and 886 cm^{-1}, respectively as compared to those modes of undoped H_2BN (1052 and 953 cm^{-1}). Such softening may contribute to the strong e-ph interaction.

We plot the Fermi surfaces of the strained H_2BN with BTS of 6% in Figs. 2(d) and 2(e), respectively, for 2.0×10^{14} and 3.4×10^{14} holes cm^{-2}. As shown, the Fermi surfaces contain hole pockets near both the high-symmetry Γ and K points. The appearance of hole pockets at K points can be attributed to the higher hole densities that can be accommodated for strained H_2BN.

E. Eliashberg function

Using Eq. (1), we compute phonon linewidths ($\gamma_{q\nu}$), which we use later for evaluating the Eliashberg function.

$$\gamma_{q\nu} = 2\pi\omega_{q\nu}\sum_{mn}\int_{BZ}\frac{dk}{A_{BZ}}|g^{\nu}_{mn}(k,q)|^2\delta(E_{k,m}-E_F) \times \delta(E_{k+q,n}-E_F), \quad (1)$$

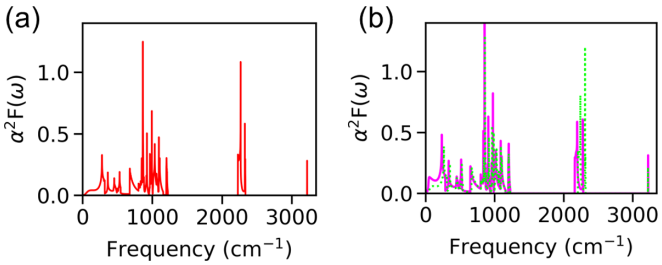

FIG. 7. Eliashberg function of hole-doped H_2BN with the carrier density of (a) 1.0×10^{14}, (b) 1.3×10^{14} (green trace), and 1.5×10^{14} holes cm^{-2} (magenta).

where $g^{\nu}_{mn}(k,q)$ is the e-ph matrix elements for an electron with momentum k and band index m and n, and for a phonon with wave vector q, branch index ν, and frequency $\omega_{q\nu}$, A_{BZ} the BZ area, δ the Dirac delta, and E_F Fermi energy. Since holes at the top of the zone-centered, σ-bonding VB couple strongly to the optical bond-stretching modes [48], the phonons corresponding to soft B-N stretching modes may strongly couple with charge carriers in the hole-doped H_2BN.

The connection between the e-ph matrix elements and the EPC is established by Eliashberg relation [42]:

$$\alpha^2F(\omega) = \frac{1}{2\pi N(E_F)}\sum_{q\nu}\delta(\omega-\omega_{q\nu})\frac{\gamma_{q\nu}}{\omega_{q\nu}}, \quad (2)$$

where $N(E_F)$ is the electronic DOS at E_F, $\gamma_{q\nu}$ [see Eq. (1)] is the phonon linewidth of mode ν with phonon momentum q and frequency $\omega_{q\nu}$, and δ the Dirac delta. Figure 7 shows the Eliashberg function of doped H_2BN that measures the relative contribution of its different modes to the superconducting pairing [42]. For the doping with 1.0×10^{14} holes cm^{-2}, the Eliashberg functions possess a maximum peak at 756 cm^{-1} [see Fig. 7(a)], closer to the Γ-point frequency of 675 cm^{-1}, that originates from the in-plane B-N stretching modes. These modes are similar to those in the p-doped graphane that has the in-plane C-C stretching and H atoms moving in phase with C atoms for both 1% and 4% dopings [16]. In the optical region, the other two peaks appear at 978 and 1079 cm^{-1}, which are associated with the H in-plane vibrations. On the circular Fermi surface near Γ point, electrons are expected to strongly couple with phonons corresponding to the B-N modes and moderately with those corresponding to the in-plane vibrations of H atoms. For the higher n at 1.5×10^{14} holes cm^{-2}, a maximum peak appears at 629 cm^{-1} [see Fig. 7(b)], closer to Γ-point frequency of 647 cm^{-1}, that is associated with B-N stretching modes, and the other two peaks at 966 and 1076 cm^{-1}, which are associated with in-plane optical modes of H atoms.

F. Electron-phonon interaction and superconducting properties

We calculate the superconducting transition temperature using the modified McMillan equation [33–35]:

$$T_c = \frac{\langle\omega_{\log}\rangle}{1.2}\exp\left[\frac{-1.04(1+\lambda)}{\lambda-\mu^*(1+0.62\lambda)}\right], \quad (3)$$

where μ^* is the Coulomb parameter (Morel-Anderson pseudopotential), the λ is given by $2\int d\omega\omega^{-1}\alpha^2F(\omega)$ [42], and

TABLE II. Hole carrier density (n in holes cm^{-2}), BTS (ϵ in percentage), electronic DOS at E_F (EDOS in states/eV), e-ph interaction parameter (λ), logarithmically averaged frequency ($\langle\omega_{\log}\rangle$ in cm^{-1}), superconducting transition temperature (T_c in Kelvin) for hole-doped H_2BN.

n ($\times 10^{14}$)	ϵ	EDOS	λ	$\langle\omega_{\log}\rangle$	T_c
0.6	0	0.42	0.61	580	14.3
1.0	0	0.61	0.72	499	20.7
1.3	0	0.69	0.81	428	24.0
1.5	0	0.86	1.10	312	31.3
1.6	6	1.00	1.20	398	45.5
2.0	6	1.06	1.67	386	64.2
2.8	6	1.11	2.25	365	76.5
3.4	6	1.32	2.75	350	82.5

$\langle\omega_{\log}\rangle$ is the logarithmically averaged phonon frequency and is given by $\exp[2\lambda^{-1}\int d\omega\omega^{-1}\alpha^2F(\omega)\ln\omega]$, with $\alpha^2F(\omega)$ being the Eliashberg spectral function, as given by Eq. (2). In atomic units, the reduced Planck's constant ($\hbar$) and Boltzmann constant (k_B) can be set to unity.

In Table II , we present the calculated T_c and the EPC λ of the doped H_2BN for different densities of hole carriers. The T_c appears to be increased from 14.3 K at n of 0.6×10^{14} holes cm^{-2} to 31.3 K at n of 1.5×10^{14} holes cm^{-2}. Within this range, both the electron DOS and λ get enhanced with the increase of n. This result shows the correlation between EPC, DOS, and robust SC [50]. In the literature, the μ^* has been taken as an empirical parameter. For metallic systems, the values of μ^* can be small (e.g., see Ref. [49]). For doped layer systems, μ^* has been chosen to be from 0.10 to 0.14 ([20,22,23]). In our work, we choose $\mu^* = 0.13$, which can be regarded as Coulomb repulsion with moderate strength. It is important to notice that doping with higher n would cause the lattice to become unstable at 1.6×10^{14} holes cm^{-2} [see Fig. 11(b) in Appendix]. The critical hole density for creating the LI is $n_c \sim 1.55 \times 10^{14}$ holes cm^{-2}. But we can stabilize the LI by applying BTS. If we take $\epsilon = 6\%$, the n that causes the LI is moved to higher density $n_c \sim 3.45 \times 10^{14}$ holes cm^{-2} (Fig. 6). In Table II, we also list the calculated T_c for doped H_2BN under BTS of 6% with several n ranged from 1.6 to 3.4 $\times 10^{14}$ holes cm^{-2}. When n approaches the value near the LI, the DOS, EPC, and T_c increase. For doped H_2BN with n of 3.4×10^{14} holes cm^{-2}, we estimate the T_c at 82.5 K. The detailed estimation of T_c is presented near the end of the Appendix (see Figs. 12–14). The T_c might be further increased by applying more BTS along with the higher doping, however, the physics regarding the phonon-mediated SC in hole-doped H_2BN will not be changed.

IV. CONCLUSIONS

In summary, we have demonstrated using first-principles DFT approaches that the p-doped H_2BN can be an e-ph superconductor. The chemical modification of monolayer h-BN by hydrogen atoms results in not only high-energy phonons but also the higher phonon DOS. The favorable doping of H_2BN by holes can form a stable lattice with strong e-ph couplings. The synergy between hydrogenation and doping plays a crucial role for SC in hole-doped H_2BN. The phonon-mediated SC with T_c of 31.3 K can be achieved for the doped H_2BN with n of 1.5×10^{14} holes cm^{-2} near the LI when $\epsilon = 0$. To understand the SC at higher n, we need to apply a BTS for pushing a critical hole density toward the higher n. At $\epsilon = 6\%$, we can dope the H_2BN with higher n up to 3.4×10^{14} holes cm^{-2} near new LI, and thereby enhance T_c up to 82.5 K. We can thus achieve the maximum T_c at hole densities near LIs. This is quite different from the case of doped h-BN, where no SC is found at $\epsilon = 0$, but T_c is estimated to be 41 K at $\epsilon = 17.5\%$ and $n = 5.3 \times 10^{14}$ holes cm^{-2} with $\mu^* = 0.10$ [20]. We applied weaker BTS and chose smaller hole densities with the expectation that they may be more accessible to experiments. Since the fully hydrogenated graphene has been realized in Ref. [51], we expect that there should be no obstacles to grow H_2BN in laboratory. We hope that phonon-mediated SC in doped H_2BN will be realized experimentally. When realized, one may exploit the doped H_2BN for nanosuperconducting quantum devices that may have potential applications in quantum information technology.

ACKNOWLEDGMENTS

This work was supported by the Texas Center for Superconductivity at University of Houston, the Robert A. Welch Foundation (Grant No. E-1146), the National Natural Science Foundation of China (Grant No. 12074213), and the Major Basic Program of Natural Science Foundation of Shandong Province (Grant No. ZR2021ZD01). We acknowledge the Research Computing Data Core (RCDC) at the University of Houston for providing the high-performance computing resources.

APPENDIX

1. Electronic density of states and symmetry operations

Figure 8 shows the electronic DOS of pristine h-BN and H_2BN monolayers. While the highest occupied electronic states are of dominantly of N $2p_z$ characters for monolayer h-BN [Fig. 8(a)], the most of the DOS of H_2BN dominantly come from B $2p_z$ and H $1s$ orbitals and partly from N $2p_x$ and $2p_y$ [Fig. 8(b)] when summing contributions for all k points. The B $2p_z$ and H1 s states are strongly hybridized with almost similar density peak in the projected DOS spectra [Fig. 8(b)]. The B $2p_z$ state which dominantly appears just above the chemical potential [Fig. 8(a)], now disappears when h-BN is fully hydrogenated [Fig. 8(b)]. So, the hydrogenation results in the significant modifications in the electronic properties of h-BN. Since the hydrogen electronic states have energy closer to the chemical potential. The suitable doping of H_2BN by holes may bring these hydrogen electronic states closer to the chemical potential.

We discuss the electronic DOS of the hole-doped H_2BN with n of 1.0×10^{14} holes cm^{-2} obtained by projection onto the atomic orbitals of B, N, and H atoms. In Fig. 9 , we show the DOS projected on B and N $2p$ orbitals and H $1s$ orbitals. The hole doping brings some electronic states at the Fermi level. These states mainly include the B $2p_z$, H $1s$, and N $2p_x$ and $2p_y$ components. Note that the resulting DOS is obtained

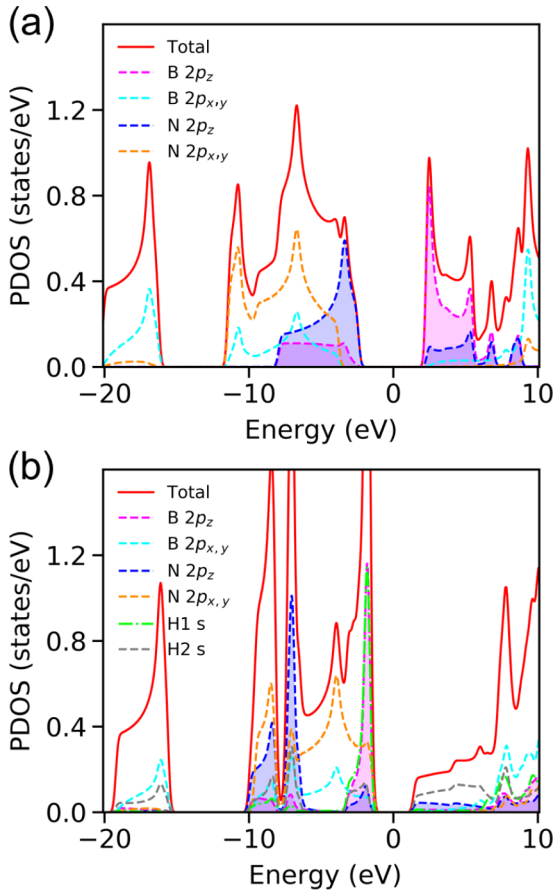

FIG. 8. Projected density of states (PDOS) of (a) monolayer *h*-BN and (b) H_2BN without doping. The chemical potential is set to zero. In (a), the B $2p_z$ state of monolayer *h*-BN is partly unfilled just above the chemical potential (pink trace) where the density of B $2p_z$ is relatively higher than that below the chemical potential. In (b), for the case of H_2BN, both B $2p_z$ and H $1s$ states dominantly contribute to the DOS just below the chemical potential, while the N and B $2p_{x,y}$ orbitals also contribute to the DOS. The contributions from $2p_x$ and $2p_y$ are added and shown as $2p_{x,y}$. Here, H1 and H2 are bonded to B and N atoms, respectively.

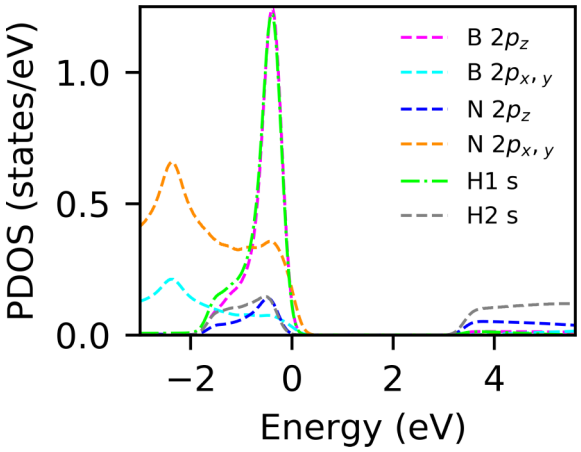

FIG. 9. Projected density of states (PDOS) of hole-doped H_2BN with a carrier density of 1.0×10^{14} holes cm^{-2}. Here, the PDOS is shown for the selected energy range from −3.0 to 5.6 eV. The Fermi level is set to zero. Within from ∼−1.8 to 0.2 eV, B $2p_z$ (magenta trace) and H1 s (green) states are strongly hybridized. The N $2p_{x,y}$ also have contributions to this hybridized state. The H1 atom which is bonded to B atom has similar PDOS near and at Fermi level to that coming from B $2p_z$ orbital.

by considering all k points in the BZ. For the Γ point resolved DOS (not shown), the major contributions arise from N $2p_x$ and $2p_y$ orbitals.

Here we also show the symmetry operations in monolayer pristine *h*-BN and H_2BN in Table III. There are 12 symmetry operations in *h*-BN and only 6 in H_2BN.

2. Vibrational properties

In Fig. 10, we show the selected optical phonon modes with corresponding frequencies that are calculated at the center of BZ of the hole-doped H_2BN with n of 1.0×10^{14} holes cm^{-2}. There exist six different optical modes. The optical modes with frequencies at 3321, 2328, and 846 cm^{-1} have polarizations nearly perpendicular to the lattice plane at the Γ point. The high-frequency modes with frequencies of 3221 and 2328 cm^{-1} are associated with the H motion nearly perpendicular to the lattice plane, but at other high symmetry points, the polarization of H-atom vibrations may not be perpendicular to the lattice plane. Our numerical results suggest that these modes of H atoms are little renormalized or suppressed by the hole doping. At the Γ point, the transverse optical mode with phonon frequency of 864 cm^{-1} associated with the motion of B and N atoms is also nearly perpendicular to the plane. At Γ, the B-N stretching mode with 675 cm^{-1} should contribute dominantly, followed by two modes with 1059 and 965 cm^{-1} associated with the in-plane motion of H atoms, to the e-ph interaction.

We now examine the dynamical stability of doped H_2BN for higher hole carrier densities. In Fig. 11 , we present the phonon frequency dispersion of doped H_2BN with carrier densities of 1.5×10^{14} and 1.6×10^{14} holes cm^{-2}. The doped H_2BN system is found dynamically stable for n of 1.5×10^{14} holes cm^{-2} [Fig. 11(a)]. But if we increase the carrier density

TABLE III. Symmetry operations in monolayer *h*-BN and H_2BN model systems. The first six symmetry operations exist in both systems, and the remaining operations only exist in the *h*-BN. The crystal axes are given in brackets.

Model systems	Symmetry operations
h-BN and H_2BN	Identity
h-BN and H_2BN	120° rotation - [0,0, 1]
h-BN and H_2BN	120° rotation - [0, 0, −1]
h-BN and H_2BN	180° rotation-inversion - [1, 0, 0]
h-BN and H_2BN	180° rotation-inversion - [0, 1, 0]
h-BN and H_2BN	180° rotation-inversion - [1, 1, 0]
h-BN	180° rotation-inversion - [0, 0, 1]
h-BN	60° rotation-inversion - [0, 0, 1]
h-BN	60° rotation-inversion - [0, 0, −1]
h-BN	180° rotation - [0, 1, 0]
h-BN	180° rotation - [1, −1, 0]
h-BN	180° rotation - [2, 1, 0]

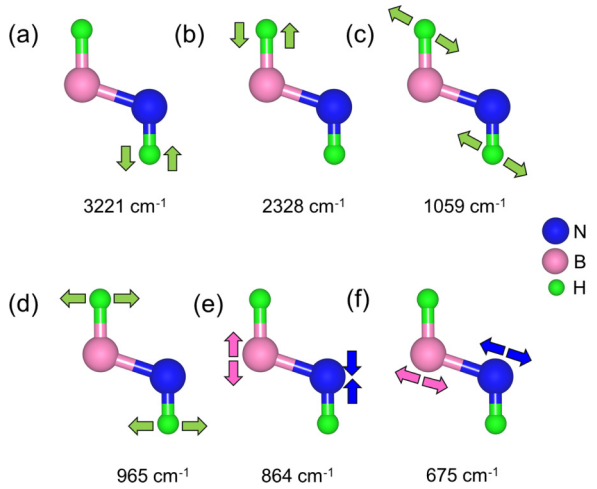

FIG. 10. Schematic representations of the selected optical phonon modes at the Γ point of Brillouin zone of the hole-doped H_2BN with a hole carrier density of 1.0×10^{14} holes cm^{-2}. The green, pink, and blue arrows indicate the motions of hydrogen, boron, and nitrogen atom, respectively.

to 1.6×10^{14} holes cm^{-2}, the lattice becomes unstable with negative frequencies appearing in one of the acoustic branches near the zone center [Fig. 11(b) and inset]. Therefore, the carrier density such as 1.55×10^{14} holes cm^{-2} could be the maximum n that can be utilized for doping holes to the unstrained H_2BN system.

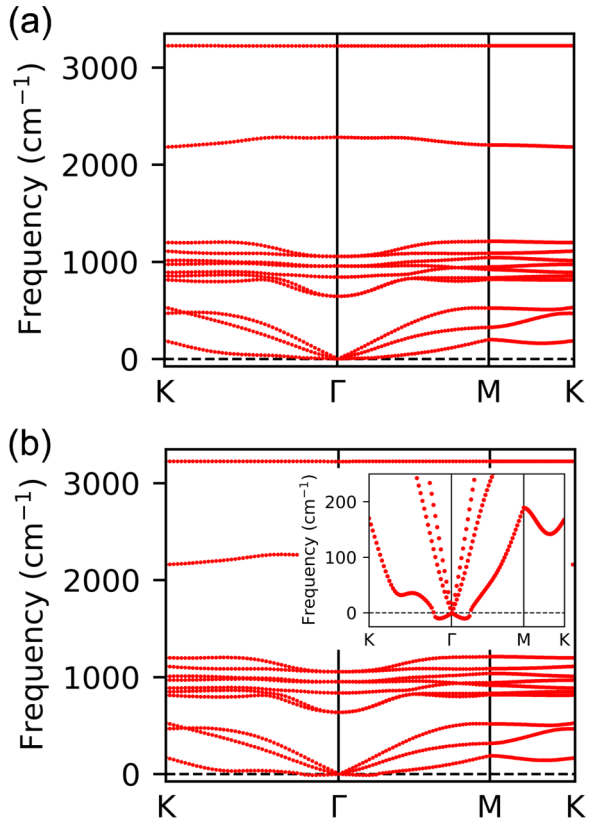

FIG. 11. Phonon frequency dispersion of the doped H_2BN with the carrier density of (a) 1.5×10^{14} and (b) 1.6×10^{14} holes cm^{-2}. For the latter hole carrier density, the doped H_2BN system has negative frequencies shown in inset.

TABLE IV. Comparison of the selected optical phonon frequencies (given in unit of cm^{-1}) at the center of Brillouin zone of undoped H_2BN (without strain) and hole-doped H_2BN systems. For the doped H_2BN, the carrier densities (in unit of 10^{14} holes cm^{-2}) are given in parenthesis. The normal modes are provided, and numbers in parenthesis represent degree rotation. The in-plane H, Out-of-plane B-N, and B-N stretching modes have E, A_1, and E′ symmetry, respectively.

Normal modes	H_2BN (0.0)	H_2BN (1.0)	H_2BN (1.5)
In-plane H (0)	1089	1059	1056
In-plane H (90)	1089	1059	1056
In-plane H (30)	971	965	956
In-plane H (120)	971	965	956
Out-of-plane B-N	946	864	843
B-N stretching (0)	850	675	647
B-N stretching (90)	850	675	647

In Table IV, we present the selected phonon frequencies with degenerate and non-degenerate modes calculated at the center of BZ of undoped and hole-doped H_2BN systems, and the corresponding normal modes of vibrations. The low-frequency optical modes which are related to H motions and the optical B-N modes are found to soften when H_2BN system is doped with n of 1.0×10^{14} holes cm^{-2}. With further increase of holes to 1.5×10^{14} holes cm^{-2}, these modes become more softer. The phonon modes thus become more softer when we increase the carrier density. The softening of the in-plane phonon modes may play an important role in enhancing the phonon-mediated superconductivity.

3. Estimation of T_c

Figures 12 and 13 show the variations of T_c as functions of the degauss parameter (Gaussian smearing for sum over q points that is not the same as used in ph.x calculations) for phonons and smearing/broadening parameter for e-ph

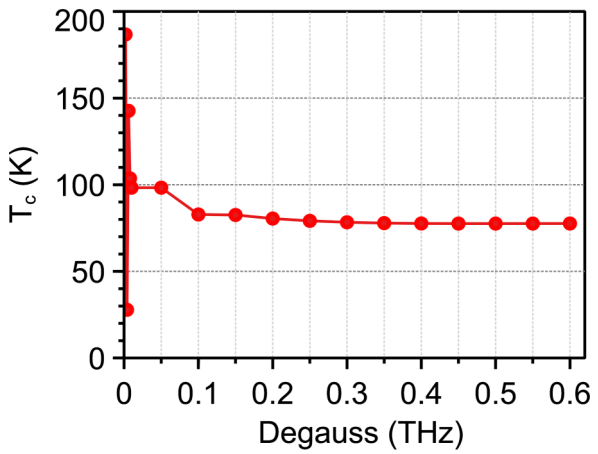

FIG. 12. Superconducting transition temperature for hole-doped H_2BN with BTS=6% and carrier density of 3.4×10^{14} holes cm^{-2} as a function of degauss for phonons.

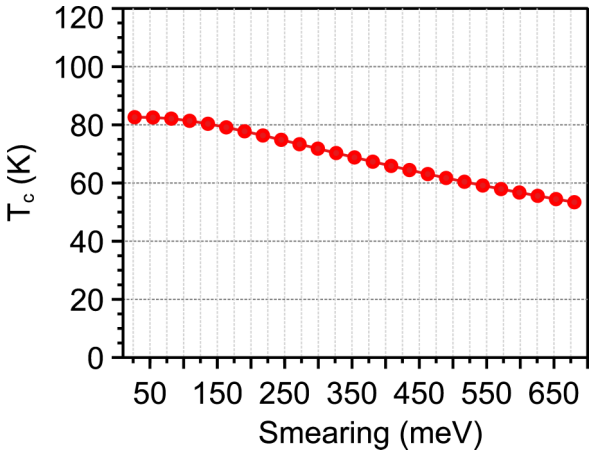

FIG. 13. Superconducting transition temperature for hole-doped H_2BN with BTS=6% and carrier density of 3.4×10^{14} holes cm^{-2} as a function of double delta smearing for e-ph interaction.

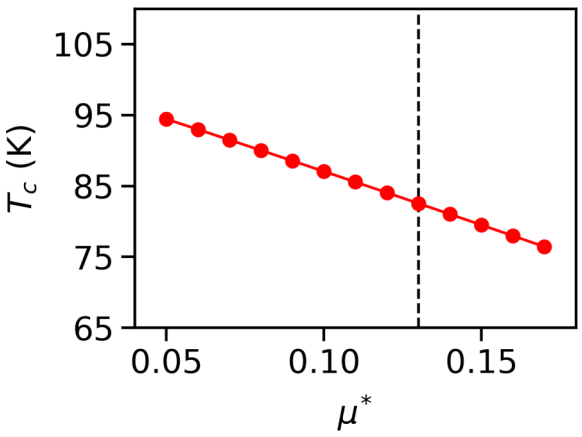

FIG. 14. The variation of T_c with μ^*. In our work, we have chosen $\mu^* = 0.13$, as indicated by the dashed line. The chosen μ^* can be regarded as Coulomb repulsion with the moderate strength.

interaction. We firstly calculate T_c at different degauss values until the results become convergent. The convergent result is shown in Fig. 12. The values of degauss in the range from 0.03 to 0.1 THz (or equivalently 1.0 to 3.3 cm^{-1}) may be sufficient to do smearing for phonon DOS. The variation in T_c as a function of the double delta smearing parameter is shown in Fig. 13 with the choice of degauss of 0.1 THz. In the mathematical expressions for the electron DOS, there exist the δ functions. To simplify numerical calculations, the δ function is usually replaced by a Lorentz distribution function with a smearing parameter. The correct limit is to choose γ_s as small as possible, and only in $\gamma_s \to 0$ limit, the Lorentzian function goes back to δ function.

The relation for μ^* is given by $\mu^* = N(E_F)V_c/(1 + N(E_F)V_c \ln(E_F/\omega_{ph}))$ [49], where E_F = Fermi energy, ω_{ph} is phonon frequency averaged over the BZ, $N(E_F)$ is the electron density of states at the Fermi level, and V_c is the Coulomb repulsion between two electrons averaged over the Fermi surface. To determine the effect of μ^* on T_c, we studied the T_c of doped H_2BN under BTS of 6% with $n = 3.4 \times 10^{14}$ holes cm^{-2} for different values of μ^* ranged from 0.05 to 0.17. We show the plot of T_c versus μ^* in Fig. 14. The T_c is found to decrease monotonically with increasing the value of μ^*. The T_c is 94.4 K when $\mu^* = 0.05$, and it reduces to $T_c = 76.4$ K when $\mu^* = 0.17$. In our work, we choose $\mu^* = 0.13$, which can be regarded as Coulomb repulsion with the moderate strength. At $\mu^* = 0.13$, the T_c is found to 82.5 K.

[1] K. S. Novoselov, A. K. Geim, S. V. Morozov, D. Jiang, Y. Zhang, S. V. Dubonos, I. V. Grigorieva, and A. A. Firsov, Science **306**, 666 (2004).

[2] K. S. Novoselov, A. K. Geim, S. V. Morozov, D. Jiang, M. I. Katsnelson, I. V. Grigorieva, S. V. Dubonos, and A. A. Firsov, Nature (London) **438**, 197 (2005).

[3] A. K. Geim and K. S. Novoselov, Nat. Mater. **6**, 183 (2007).

[4] S. V. Morozov, K. S. Novoselov, M. I. Katsnelson, F. Schedin, D. C. Elias, J. A. Jaszczak, and A. K. Geim, Phys. Rev. Lett. **100**, 016602 (2008).

[5] A. H. Castro Neto, F. Guinea, N. M. R. Peres, K. S. Novoselov, and A. K. Geim, Rev. Mod. Phys. **81**, 109 (2009).

[6] V. N. Kotov, B. Uchoa, V. M. Pereira, F. Guinea, and A. H. Castro Neto, Rev. Mod. Phys. **84**, 1067 (2012).

[7] S. Li, J. Li, Y. Wang, Ch. Yu, Y. Li, W. Duan, Y. Wang, and J. Zhang, Nat. Electron. **4**, 254 (2021).

[8] J.-J. Wang *et al.*, Nat. Nanotechnol. **14**, 120 (2019).

[9] J. M. Park, Y. Cao, K. Watanabe, T. Taniguchi, and P. J.-Herrero, Nature (London) **590**, 249 (2021).

[10] Z. Hao, A. M. Zimmerman, P. Ledwith, E. Khalaf, D. H. Najafabadi, K. Watanabe, T. Taniguchi, A. Vishwanath, and P. Kim, Science **371**, 1133 (2021).

[11] Y. Cao, V. Fatemi, S. Fang, K. Watanabe, T. Taniguchi, E. Kaxiras, and P. Jarillo-Herrero, Nature (London) **556**, 43 (2018).

[12] Y. Cao, V. Fatemi, A. Demir, S. Fang, S. L. Tomarken, J. Y. Luo, J. D. Sanchez-Yamagishi, K. Watanabe, T. Taniguchi, E. Kaxiras, R. C. Ashoori, and P. Jarillo-Herrero, Nature (London) **556**, 80 (2018).

[13] M. Topsakal, E. Aktürk, and S. Ciraci, Phys. Rev. B **79**, 115442 (2009).

[14] H. J. Park, J. Cha, M. Choi, J. H. Kim, R. Y. Tay, E. H. T. Teo, N. Park, S. Hong, and Z. Lee, Sci. Adv. **6**, eaay4958 (2020).

[15] G. Profeta, M. Calandra, and F. Mauri, Nat. Phys. **8**, 131 (2012).

[16] G. Savini, A. C. Ferrari, and F. Giustino, Phys. Rev. Lett. **105**, 037002 (2010).

[17] B. M. Ludbrook *et al.*, Proc. Natl. Acad. Sci. USA **112**, 11795 (2015).

[18] J. Lu, O. Zheliuk, I. Leermakers, N. F. Yuan, U. Zeitler, K. T. Law, and J. Ye, Science **350**, 1353 (2015).

[19] H. Y. Lu *et al.*, Phys. Rev. B **101**, 214514 (2020).

[20] X. T. Jin, X. W. Yan, and M. Gao, Phys. Rev. B **101**, 134518 (2020).

[21] C. Si, Z. Liu, W. Duan, and F. Liu, Phys. Rev. Lett. **111**, 196802 (2013).

[22] N. H. Shimada, E. Minamitani, and S. Watanabe, J. Phys.: Condens. Matter **32**, 435002 (2020).
[23] N. H. Shimada, E. Minamitani, and S. Watanabe, Appl. Phys. Express **10**, 093101 (2017).
[24] K. A. Szewczyk, I. A. Domagalska, A. P. Durajski, and R. Szczesniak, Beilstein J. Nanotechnol. **11**, 1178 (2020).
[25] J. P. Perdew and A. Zunger, Phys. Rev. B **23**, 5048 (1981).
[26] D. R. Hamann, M. Schluter, and C. Chiang, Phys. Rev. Lett. **43**, 1494 (1979).
[27] G. Kresse and J. Hafner, J. Phys.: Condens. Matter **6**, 8245 (1994).
[28] J. Kohanoff, *Electronic Structure Calculations for Solids and Molecules: Theory and Computational Methods* (Cambridge University Press, Cambridge, 2006).
[29] S. Baroni, S. de Gironcoli, A. Dal Corso, and P. Giannozzi, Rev. Mod. Phys. **73**, 515 (2001).
[30] J. Bardeen, L. N. Cooper, and J. R. Schrieffer, Phys. Rev. **108**, 1175 (1957).
[31] G. M. Eliashberg, Sov. Phys. JETP **11**, 696 (1960).
[32] W. L. McMillan, Phys. Rev. **167**, 331 (1968).
[33] P. B. Allen and R. C. Dynes, Phys. Rev. B **12**, 905 (1975).
[34] P. B. Allen and B. Mitrovi, Solid State Phys. **37**, 1 (1983).
[35] F. Marsiglio and J. Carbotte, *Superconductivity* (Springer-Verlag, Berlin, Heidelberg, 2008).
[36] P. Giannozzi *et al.*, J. Phys.: Condens. Matter **29**, 465901 (2017).
[37] G. Kern, G. Kresse, and J. Hafner, Phys. Rev. B **59**, 8551 (1999).
[38] I. Hamdi and N. Meskini, Phys. B: Condens. Matter **405**, 2785 (2010).
[39] M. Methfessel and A. T. Paxton, Phys. Rev. B **40**, 3616 (1989).
[40] H. J. Monkhorst and J. D. Pack, Phys. Rev. B **13**, 5188 (1976).
[41] J. Noffsinger, F. Giustino, S. G. Louie, and M. L. Cohen, Phys. Rev. B **79**, 104511 (2009).
[42] G. Grimvall, *The Electron-Phonon Interaction in Metals* (North-Holland, New York 1981).
[43] J. O. Sofo, A. S. Chaudhari, and G. D. Barber, Phys. Rev. B **75**, 153401 (2007).
[44] V. L. Solozhenko, G. Will, and F. Elf, Solid State Commun. **96**, 1 (1995).
[45] J. Bekaert, M. Petrov, A. Aperis, P. M. Oppeneer, and M. V. Milosevic, Phys. Rev. Lett. **123**, 077001 (2019).
[46] W. Kohn, Phys. Rev. Lett. **2**, 393 (1959).
[47] F. Giustino, Rev. Mod. Phys. **91**, 019901(E) (2019).
[48] L. Boeri, J. Kortus, and O. K. Andersen, Phys. Rev. Lett. **93**, 237002 (2004).
[49] C. F. Richardson and N. W. Ashcroft, Phys. Rev. Lett. **78**, 118 (1997).
[50] Y. W. Choi and H. J. Choi, Phys. Rev. Lett. **127**, 167001 (2021).
[51] J. Son, S. Lee, S. J. Kim, B. C. Park, H.-K. Lee, S. Kim, J. H. Kim, B. H. Hong, and J. Hong, Nat. Commun. **7**, 13261 (2016).